THE ASTROPHYSICAL JOURNAL, 449:365–375, 1995 August 10

INTERFEROMETRIC OBSERVATIONS OF THE SiO MASERS AND DUST SHELL OF VX SAGITTARII

L. J. GREENHILL, F. COLOMER,[1] AND J. M. MORAN
Harvard-Smithsonian Center for Astrophysics, 60 Garden Street, Cambridge, MA 02138
D. C. BACKER
Department of Astronomy, University of California, Berkeley, CA 94720
AND
W. C. DANCHI AND M. BESTER
Space Sciences Laboratory, University of California, Berkeley, CA 94720
Received 1994 July 18; accepted 1995 February 17

ABSTRACT

We report the results of VLBI observations at 7 mm wavelength of the SiO maser emission ($J = 1 \rightarrow 0$, $v = 1$) in the circumstellar envelope of the late-type variable star VX Sagittarii. These are the first VLBI observations that have been coordinated with mid-infrared interferometric observations of late-type stars. Synthesis images show that the maser emission at a stellar phase of about 0.4 arises from a ringlike distribution with a radius of about 1.3 R_*. The distribution of emission is asymmetric and the strongest emission arises from the redshifted center of activity that lies to the south of the star. This may indicate an asymmetry in the mass-loss or stellar atmosphere. The maser emission within 4 km s^{-1} of the stellar velocity is distributed around the stellar limb and does not show evidence of systematic velocity gradients greater than a few km s^{-1}. The overlap of maser features is consistent with outflow (or infall) of material away from (or toward) the star of about 10 km s^{-1} at 1.3 R_*, about half the velocity observed in the OH and H_2O maser shells at radii of greater than 30 R_*.

The arrangement of the maser emission suggests the presence of dense velocity coherent structures with characteristic sizes of $\sim$0.4 AU (0.02 R_*) in the extended atmosphere above the photosphere. However, 74% of the maser flux was resolved by these observations, as with earlier, single-baseline VLBI observations of coarser angular resolution. We speculate that the circumstellar shell also has velocity coherent cells on spatial scales of 30 to perhaps 100 AU, which give rise to SiO maser emission.

The compact SiO maser emission lies well within the 4.6 R_* inner radius of the circumstellar dust shell, as measured with the UC Berkeley Infrared Spatial Interferometer at about the same stellar minimum. The stellar radius at stellar minimum was measured to be 22 ± 3 AU (13 ± 2 mas). Infrared observations made close to stellar maximum show an inner radius of 6.0 R_*. The estimated density at the inner edge of the dust shell, the location of the masers, and the density at which the maser levels probably thermalize are consistent with models of atmospheric extension due to pulsation-driven shocks.

Subject headings: circumstellar matter — masers — stars: individual (VX Sgr) — techniques: interferometric

1. INTRODUCTION

The geometry and dynamics of the circumstellar envelopes associated with late-type stars are determined by the stellar mass loss. Important insights can be obtained by studying the envelopes of these stars with angular resolutions commensurate with the radii at which dust forms. Many previous studies have been unable to attain sufficient angular resolution because of limitations imposed by astronomical seeing. However, many circumstellar envelopes harbor radio beacons in the form of OH, H_2O, and SiO masers, which make the shells suitable subjects for radio interferometric observations at high angular resolution ($\ll 1''$). In addition, recently developed interferometric techniques at optical and infrared wavelengths (e.g., speckle, aperture masking, and heterodyne interferometry) now permit angular resolutions much less than the diameters of the envelopes (Haniff et al. 1992; Wilson et al. 1992; Danchi et al. 1994).

Maser emission is thought to arise from velocity coherent "cloudlets." These cloudlets may be distinct density enhancements moving ballistically in the mass flows around the star, as are many H_2O masers in regions of star formation (Reid & Moran 1988). Alternatively, the masers may be regions of relatively low density contrast, which are limited in extent by the coherence of the velocity field. The characteristic temperatures of the vibrationally excited stars for the SiO emission (> 1000 K) require that it arise closer to the star than H_2O or OH emission. Hence, the presence of SiO masers provides a means of studying the inner parts of circumstellar envelopes. Beyond the radius at which silicate dust condenses in a circumstellar shell, nearly all the gas-phase silicon is expected to be incorporated into dust grains and the SiO maser emission quenched. The dust around some cool giant and supergiant stars is expected to form within a few stellar radii of the stellar photospheres ($\lesssim 1000$ K).

[1] Current address: Centro Astronómico de Yebes, Apartado 148, 19080 Guadalajara, Spain.

Neither the ideas about the relative locations of the circumstellar SiO masers and circumstellar dust nor the self-consistency of the inferred physical conditions have been well tested. The first-generation maps of the distribution of SiO maser emission ($J = 1 \rightarrow 0, v = 1$) were made for VY CMa, VX Sgr, and R Cas (Moran et al. 1979; Lane 1982, 1984; McIntosh et al. 1989). These early very long baseline interferometer (VLBI) observations utilized the 74 km baseline linking the Haystack Observatory and the Five College Radio Astronomy Observatory (i.e., fringe spacing 20 mas). These experiments showed that at each line-of-sight velocity the SiO masers consisted of individual compact emission features, clustered in a region of radius equal to a few stellar radii. While the correlated flux densities of some spectral lines were as high as 70% of their total-power flux densities, much of the emission appeared to be resolved. Colomer et al. (1992) obtained visibilities of 0.1–1.0 on projected baselines of ~330–1740 km, and estimated the angular sizes of spectral components to be less than 0.4–3 mas, for 10 sources between 240 and 1500 pc in distance. Most recently, Diamond et al. (1994) have generated synthesis images of SiO masers associated with TX Cam and U Her, though these are not strong infrared sources and little is known about their dust shells. Miyoshi et al. (1994) have also mapped the maser brightness distribution for W Hya and VY CMa.

We present a study of the M supergiant VX Sgr, which is a semiregular variable that fluctuates between spectral-type M4 eIa and M9.5 with a mean period of 732 days (Kholopov et al. 1987). It is one of the latest spectral types that has been observed. The distance to VX Sgr is uncertain by a factor of 4. Humphreys, Stecker, & Ney (1972) suggest that VX Sgr is a member of the Sgr OB6 association, whose distance is estimated to be 1.7–2.0 kpc (Alter, Balázs, & Ruprecht 1970, and references therein). The star lies within 6° of the nominal position of the association. However, there are no compelling reasons to expect that this late-type star is associated with this OB association. Furthermore, Humphreys (1974) estimates from photometry a distance of 0.8–1.3 kpc, depending upon the uncertain visual extinction along the line of sight, while Loup et al. (1993) estimate a distance of about 400 pc based on the canonical luminosity for AGB stars. VX Sgr would probably not be classified as a supergiant star if it were at this nearest distance. To facilitate calculations and comparisons, we assume a distance of 1.7 kpc.

At the assumed distance, VX Sgr is one of the most luminous stars known, with $L_* \sim 4.2 \times 10^5\ L_\odot$ (Humphreys 1974). From lunar occultation measurements (Ridgway, Wells, & Joyce 1977) and blackbody models applied to photometric data (e.g., Danchi et al. 1994), the radius is estimated to be about 13 mas, or 22 AU. The mass-loss rate for the star has been computed to be between 10^{-4} and $10^{-5}\ M_\odot\ \mathrm{yr}^{-1}$ (Danchi et al. 1994; Pijpers 1990), based on the intensities of molecular or dust emissions and associated flow velocities. Chapman & Cohen (1986) estimate the systemic velocity of VX Sgr to be $5.3 \pm 0.4\ \mathrm{km\ s}^{-1}$ based on a dynamical model of an expanding envelope fit to interferometric maps of OH maser emission at 1612 MHz. This agrees reasonably well with a prior estimate of $7.3 \pm 1\ \mathrm{km\ s}^{-1}$ by Dickinson et al. (1978) derived from the centroid of the thermal SiO emission-line profiles. From optical spectroscopy, estimates of the photospheric velocity vary with time by about $\pm 10\ \mathrm{km\ s}^{-1}$ with respect to the stellar velocities inferred radio observations (Wallerstein & Fawley 1980; Wallerstein 1977). We adopt a systemic velocity of $5.3\ \mathrm{km\ s}^{-1}$.

Our study addresses the physical conditions of the innermost portions of the circumstellar shell of VX Sgr as revealed by synthesis imaging at 7 mm wavelength, using the Very Long Baseline Array (VLBA) of the National Radio Observatory (NRAO),[2] and data obtained from interferometry at 11.15 μm wavelength, using the Infrared Spatial Interferometer (ISI) of the University of California, Berkeley. In § 2 we discuss the VLBA observations of SiO emission and in § 3 discuss elements and limitations of the calibration. In § 4 we present the results of the observations. We conclude with a discussion of the structure of the dust shell (§ 5.1) as deduced from the infrared observations and the impact of the combined infrared and millimeter observations on the models of structure of the SiO maser shell (§§ 5.2 and 5.3). A preliminary analysis of these data was given by Greenhill et al. (1994).

2. VLBA OBSERVATIONS

Long-baseline observations of the VX Sgr SiO maser emission were conducted for 6 hr on 1992 August 15. They were made during a VLBA observation of the radio continuum source in the Galactic center, Sgr A* (Backer et al. 1993). The nearly simultaneous observations of a strong maser nearby in angle to Sgr A* were made to assist in the measurement of the time-varying sensitivities of the individual stations. Five stations of the partially completed VLBA participated. The stations and their performance parameters are listed in Table 1. The variation in the performance of the stations was due to the fact that the VLBA was employed early in its operations, before the stations had been optimized for such high-frequency observations (e.g., high system temperature at the Owens Valley station), and because of poor weather at the Pie Town and Los Alamos sites. The lengths of the 10 baselines among the five stations were between 237 and 2328 km. As shown in Figure 1, the projected baseline lengths ranged from 72 to 2323 km (providing fringe spacings of about 20–0.6 mas).

All stations were equipped with left circularly polarized feeds. We observed VX Sgr for 1 minute several times each hour, for a total integration time of about 1.3 baseline hours. Supplementary scans of NRAO 530 and 3C 345 were used for clock and bandpass calibration, and for fringe searching. Although the integration time was short, the relatively large number of baselines, the range of hour angles, and the source strength combined to make this VLBI snapshot the most extensive observation of VX Sgr reported yet (see Lane 1984 and Colomer et al. 1992).

TABLE 1

VLBI ARRAY

VLBA Telescope	Diameter (m)	Effective T_{sys}[a] (Jy)
Pie Town (PT)	25	3000
Los Alamos (LA)	25	4000
Kitt Peak (KP)	25	2000
Owens Valley (OV).....	25	6000
N. Liberty (NL).....	25	3000

[a] Characteristic effective system temperature near transit, at about 30°–35° elevation. For each station, the value is the system temperature multiplied by the sensitivity of the telescope in units of $\mathrm{Jy\ K}^{-1}$. The wide variation is primarily a consequence of poor subreflector positioning and hence reductions in gain during the shakedown phase of the VLBA. The absolute scale is uncertain by 20%.

[2] The NRAO is operated by Associated Universities, Inc., under cooperative agreement with the National Science Foundation.

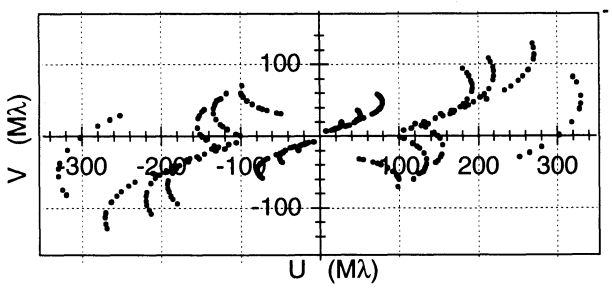

FIG. 1.—The distribution of visibility data in the (u, v)-plane. Projected baseline lengths are between 72 and 2323 km. The baselines in order of increasing length are PT–LA, PT–KP, LA–KP, KP–OV, PT–OV, LA–OV, LA–NL, PT–NL, KP–NL, and OV–NL. The station identifications are defined in Table 1.

For each scan, we recorded a single 4 MHz (27.8 km s^{-1}) bandpass (Mark III mode B), which was centered at a velocity of 10 km s^{-1} with respect to the local standard of rest (LSR). The bandpass was broad enough to cover all spectral components stronger than ≈ 30 Jy that were observed by Lane (1982) and Martínez, Bujarrabal, & Alcolea (1988), and more recently by Alcolea (1993).

3. CALIBRATION OF VLBA DATA

The data were correlated by the Mark IIIA correlator at the Haystack Observatory,[3] with an accumulation time of 4 s. Autocorrelation and cross-correlation functions were produced for VX Sgr and the two continuum calibration sources. These correlations were Fourier-transformed to provide spectra with channel spacings of 0.50 km s^{-1} and 0.25 km s^{-1} in total and cross power, respectively.

Prior to the construction of images, the visibility data were calibrated in amplitude, delay, and phase. Details of this process are discussed by Reid et al. (1980) and Greenhill et al. (1993). We obtained the amplitude calibration by estimating the scaling factors necessary to best fit a time series of total power spectra for each station to a single calibrated total power spectrum (template). A spectrum from the Kitt Peak telescope near transit was selected as the template spectrum. The flux density calibration of this template spectrum depends on the estimate of system temperature and the atmospheric extinction at that time. An opacity of 0.09 ± 0.01 and a receiver temperature of 80 K were estimated from the variation in system temperature with zenith angle over the duration of the experiment. Referenced to outside the atmosphere, the peak flux density of the maser was ~ 95 Jy (Fig. 2). The estimated peak flux density is consistent with measurements made independently with the 13.7 m Yebes telescope (Alcolea 1993). Errors in the absolute amplitude calibration make the overall flux density scale of the synthesized images uncertain by about 20%.

The delay calibration included the tasks of refining a priori station clocks, source positions, and station positions that were used by the correlator, through the use of observations of unresolved radio continuum sources. Since the Sgr A* observations required that we record data on the continuum calibrators over a 56 MHz bandwidth, we were able to use group delays

[3] Radio astronomy at the Haystack Observatory of the Northeast Radio Observatory Corporation is supported by the National Science Foundation.

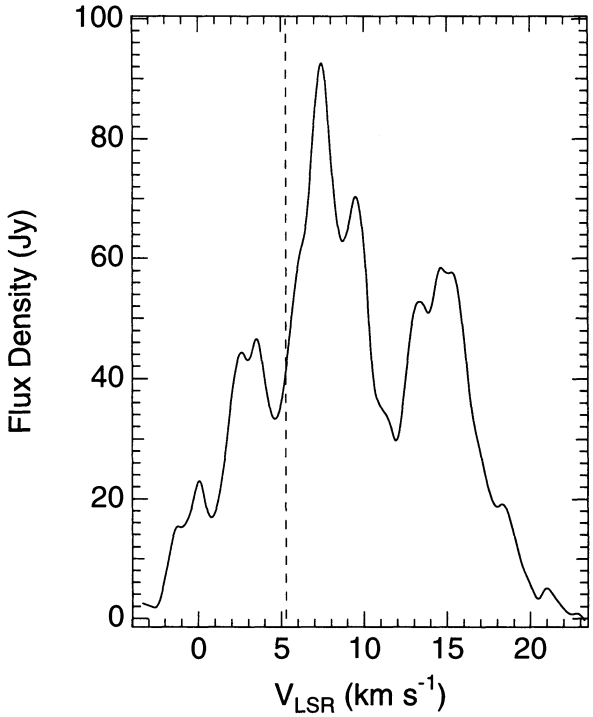

FIG. 2.—Total-power spectrum of the SiO maser associated with VX Sgr on 1992 August 15, computed from autocorrelations for the data from the Kitt Peak antenna. The integration time was 6.5 minutes on source. The flux density calibration is accurate to $\sim 20\%$ and the spectrum is referenced to outside the atmosphere. Velocities are with respect to the local standard of rest. The dashed line denotes the adopted stellar velocity of 5.3 km s^{-1}.

and estimate the clock drift rates with a precision of ~ 5 ns d^{-1}. (The drift rate for each baseline was computed and a χ^2 analysis was used to transform them into a set of relative drift rates for individual station clocks.)

The station clock offsets for the spectral-line band were obtained with an accuracy of ~ 3 ns after the drift rates were removed from the data. This hybrid solution, which employs both wide-band and narrow-band delays, can provide station clocks that are almost an order of magnitude more precise than those that rely on only narrow-band delays. We adopted the maser source position measured by Wright et al. (1990), which is accurate to 0".15. Due to the rapid atmospheric phase fluctuations and brevity of the scans, no analysis of VLBI fringe rates for the maser from our data was possible to improve this position. We adopted the station positions reported by Eubanks & Walker (1993), which are accurate to a few cm.

In order to remove the effects of the phase fluctuations due to the atmosphere and frequency standards we self-calibrated the data with the NRAO AIPS package. It was necessary to identify a reference channel with high signal-to-noise ratio (S/N) and simple structure to use to construct a source model. We analyzed the time variation of cross-spectrum amplitude for several strong spectral channels on different baselines and selected the channel at 10.25 km s^{-1} to be the reference. The self-calibration calculation began with a point source model and included four iterations, of which only the last was a solution for both phase and amplitude corrections. A solution interval of 12 s was chosen to assure adequate S/N and to avoid the decorrelation effects of the atmosphere. The rms

deviation of the final phase-only antenna solutions was 4°.5 for the five stations. The final image of the reference emission showed only a slightly resolved point source (half-power width $\lesssim$0.2 mas) of strength 21 Jy. No other structure in the image was seen above a level of about 1.8 Jy (5 σ). The amplitude and phase solutions estimated for the reference channel were applied to the rest of the spectral channels to complete the calibration. In the context of this experiment, the technique of self-calibration is similar to the technique of phase referencing as discussed by Thompson, Moran, & Swenson (1986, p. 369). However, since it was not possible to be certain of the point–source-like structure for the reference emission, as a consequence of limited S/N, self-calibration was used instead of phase referencing.

As explained in detail by Greenhill et al. (1993), residual systematic delay errors in data prior to self-calibration (or phase referencing) induce second-order position errors in synthesized images. The position error is proportional to the difference in video frequency between a maser features and the reference channel. For the error budgets of the clock and phase calibrations for this experiment, the 1 σ systematic position errors were estimated to be $\sim$1.4 and 7.2 μas km^{-1} s or $\sim$10 and 50 μas MHz^{-1} in right scensin and declination, respectively. These errors were derived from an analysis of known calibration uncertainties, the distribution of data among the baselines, and the weights given to data on the various baselines.

4. RESULTS

4.1. *Images of the Circumstellar* SiO *Maser Shell*

We constructed synthesis images of the SiO maser emission and deconvolved the synthesized beam (i.e., point source response) using the AIPS package. We weighted the individual (u, v) data points (calibrated in janskys) by the square of their relative S/Ns, based on the station sensitivities derived from fits to the template spectrum. We constructed synthesis images of the field within $\pm$50 mas of the reference maser emission for velocities between -3.9 and 23.9 km s^{-1}. The 1 σ noise level in these images was 0.4 Jy beam^{-1}. The primary beam had a width of 2.6 $\times$ 0.5 mas in half-power (FWHM) at a position angle of $-17°$. The greatest sidelobe had a relative amplitude of about 60%. We employed a broader beam to search for significant emission within $\pm$200 mas ($\pm$350 AU) of the reference with the sensitivity reduced by a factor of about 2. No additional masers were found.

The positions, mean velocities, and line widths of individual maser features were estimated by fitting three-dimensional elliptical Gaussian models in position and velocity to the images. This technique is superior to the procedure of fitting separate two-dimensional positional Gaussian models to the data for each spectral channel, after which the positions are averaged to yield a feature position. When multiple features are blended (i.e., separated by less than about one beamwidth and less than a few line widths), the simultaneous fitting in position and velocity substantially reduces biases in position, mean velocity, and line width that arise from the overlap of spectral lines. The position-velocity fitting is also better able to detect weak maser features blended with relatively stronger ones (Colomer, Menten, & Reid 1995). The residual flux densities were less than about 6 σ after subtraction of the models from the data. The cumulative reduced χ^2 value for all of the Gaussian fits was $\sim$1.1. Each data point was weighted by the 1 σ noise in the image for the corresponding spectral channel.

The estimated uncertainty in the position of a Gaussian model compared well to the statistical prediction of $0.5\Theta_B(\Delta F_\nu/F_\nu)$, where F_ν is the peak flux density, ΔF_ν is the 1 σ noise in an image of one spectral channel averaged over one line width, and Θ_B is the half-power width of the synthesized beam. The fitted uncertainties were corrected for the correlation of intensities among image pixels across the beam. For right ascension and declination this was done by multiplying the uncertainties by the square root of half the beamwidth expressed in units of pixels. Total position uncertainties were estimated by combining, in quadrature, the statistical uncertainties and systematic errors (1.4 and 7.2 μas per km s^{-1} offset from the reference frequency in right ascension and declination, respectively).

The positions of the 36 SiO maser features we detected are listed in Table 2 and plotted in Figure 3. Some of these features are blended in position and velocity. The decomposition of a part of the maser line profile into separate Gaussian components that correspond to separate spatial components is shown in Figure 4. A comparison of the fitted position errors and the statistical prediction of those errors based on the S/N confirm the consistency of the Gaussian fitting procedure.

The angular distribution of the masers resembles an irregular ring. The greatest separation among features is about 35

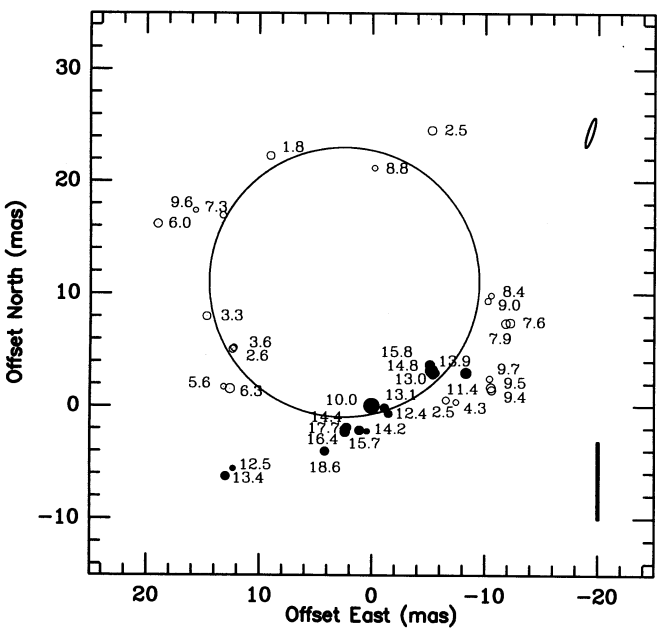

FIG. 3.—Map of the maser brightness distribution. Each maser feature is represented by a circle, the area of which is proportional to its peak flux density at the fitted center velocity, and labeled by this velocity in km s^{-1}. Maser emission that lies within 4.5 km s^{-1} of the stellar velocity is represented by open circles, and emission beyond 4.5 km s^{-1} is represented by filled circles. The disk of the star is represented by the 26 mas diameter circle (44 AU at a distance of 1700 pc). In the absence of precise optical and radio astrometry, the stellar disk is assumed to be concentric with the distribution of maser features. The astrometric positions are known only to about 0".1. The roughly concentric placement of the stellar disk and maser shell is consistent with these positions. The relative position errors of the masers are all less than 0.15 mas (see Table 1) and the angular sizes of the masers are $\sim$0.2 mas. The scale bar corresponds to 10 AU and the synthesized beam is shown in the upper right corner. Note that the features shown here account for only 26% of the total flux density of the maser. We detected all compact features stronger than 3 Jy that lie within $\pm$50 mas of the reference emission at 10.25 km s^{-1}.

TABLE 2

RELATIVE POSITIONS OF SiO MASER FEATURES FOR VX SAGITTARII

V_{lsr}[a] (km s^{-1})	σ_V	Peak F_ν (Jy)	σ_{F_ν}	$\Delta\alpha$[b] (mas)	$\sigma_{\Delta\alpha}$	$\Delta\delta$[b] (mas)	$\sigma_{\Delta\delta}$	FWHM[c] (km s^{-1})	σ_{FW}	Luminosity[d] (10^{-6} $L_\odot$)
1.806.....	0.004	6.28	0.05	9.086	0.012	22.261	0.066	0.928	0.008	0.75
2.502.....	0.003	7.42	0.05	−5.264	0.011	24.572	0.058	1.014	0.007	0.97
2.515.....	0.005	4.66	0.05	−6.570	0.011	0.542	0.064	1.050	0.012	0.63
2.565.....	0.021	5.01	0.06	12.340	0.011	5.052	0.062	1.388	0.035	0.90
3.326.....	0.003	6.09	0.05	14.677	0.010	7.977	0.058	0.792	0.008	0.62
3.593.....	0.012	4.61	0.16	2.229	0.011	5.179	0.064	0.924	0.021	0.55
4.264.....	0.048	3.47	0.06	−7.460	0.010	0.369	0.060	2.060	0.076	0.93
5.586.....	0.010	3.36	0.04	13.113	0.009	1.714	0.049	1.739	0.023	0.76
6.022.....	0.002	6.83	0.07	19.048	0.008	16.179	0.047	0.464	0.005	0.41
6.257.....	0.003	8.46	0.04	12.538	0.005	1.545	0.032	1.350	0.008	1.48
7.325.....	0.002	12.54	0.06	15.705	0.004	17.378	0.026	0.671	0.004	1.09
7.617.....	0.003	7.65	0.10	−12.263	0.007	7.424	0.034	0.776	0.007	0.77
7.884.....	0.005	6.88	0.09	−11.867	0.007	7.369	0.033	0.959	0.009	0.85
8.438.....	0.013	3.31	0.09	−10.581	0.013	9.860	0.074	0.686	0.023	0.29
8.848.....	0.009	3.20	0.04	−0.167	0.006	21.185	0.042	1.650	0.024	0.68
8.974.....	0.009	3.77	0.12	−10.274	0.014	9.374	0.074	0.581	0.016	0.28
9.403.....	0.003	6.61	0.07	−10.594	0.005	1.426	0.035	0.657	0.007	0.56
9.456.....	0.003	7.82	0.06	−10.532	0.004	1.650	0.026	0.716	0.006	0.73
9.616.....	0.003	3.97	0.06	13.286	0.007	16.949	0.050	0.722	0.012	0.37
9.667.....	0.006	4.02	0.07	−10.439	0.007	2.459	0.056	0.766	0.012	0.40
10.047[e].....	0.001	23.70	0.05	0.007	0.001	0.016	0.008	0.875	0.002	2.69
11.350	0.002	11.06	0.05	−8.332	0.003	2.972	0.020	0.906	0.005	1.30
12.393	0.004	5.88	0.05	−1.480	0.006	−0.687	0.036	0.871	0.009	0.66
12.523	0.014	3.17	0.03	12.328	0.006	−5.598	0.037	3.061	0.032	1.26
13.032	0.003	8.66	0.08	−5.417	0.006	2.856	0.034	0.564	0.006	0.63
13.130	0.004	7.22	0.04	−1.142	0.005	−0.173	0.030	1.474	0.010	1.40
13.407	0.003	7.04	0.06	12.960	0.007	−6.287	0.040	0.588	0.006	0.54
13.884	0.005	6.90	0.05	−5.636	0.006	2.964	0.038	0.994	0.015	0.89
14.220	0.006	3.31	0.05	0.426	0.010	−2.269	0.066	0.809	0.015	0.35
14.388	0.007	8.18	0.04	2.239	0.006	−1.912	0.036	1.572	0.014	1.67
14.767	0.002	15.36	0.06	−5.304	0.007	3.163	0.036	0.952	0.005	1.89
15.665	0.003	8.10	0.04	1.091	0.008	−2.167	0.045	1.221	0.008	1.28
15.789	0.004	8.72	0.05	−5.183	0.008	3.695	0.046	1.020	0.008	1.15
16.422	0.011	9.12	0.06	2.382	0.009	−2.303	0.049	1.727	0.027	2.04
17.703	0.012	5.09	0.13	2.459	0.012	−2.059	0.065	1.295	0.020	0.85
18.646	0.003	8.16	0.05	4.183	0.012	−4.022	0.066	0.893	0.006	0.94

[a] Fitted mean velocity of maser feature.
[b] Fitted relative position of feature is computed for the epoch of observation.
[c] Fitted full width at half power of maser feature.
[d] Isotropic luminosity based on a distance of 1.7 kpc and fitted FWHM.
[e] Reference velocity channel is in this feature.

mas, which we adopt as the diameter of the ring because the smaller separations among features can be attributed to projection effects. The distribution of emission around the ring is asymmetric, marked by an intense redshifted center of activity to the south, which may indicate asymmetry in the stellar atmosphere or in the mass loss. However, if we consider only emission within ± 4.5 km s^{-1} of the stellar velocity of 5.3 km s^{-1}, then the asymmetry is reduced and no systematic velocity gradients are apparent.

In Figure 5 we compare the sum of the flux densities for all the maser emission in each spectral channel (i.e., the total imaged power) to the total power spectrum of the maser. The fraction of total power imaged is between 0.1 and 0.6. Analysis of the fringe amplitudes for different maser features as a function of projected baseline length shows that a substantial amount of flux density is resolved at even the shortest baselines. However, for the available sampling of baselines the images show the partially resolved cores of maser emission (Fig. 6). The fringe amplitudes for the strongest features, which are reduced by less than 35% on the longest baselines, have angular sizes (FWHM) of $\sim$0.2 mas or $\sim$0.4 AU, based on a model Gaussian brightness distribution. The brightness temperature of the reference maser emission is $\sim 2 \times 10^{11}$ K. (We note that recent VLBI observations by us at 3 mm wavelength of the $J = 2 \rightarrow 1$, $v = 1$ transition with a projected baseline of about 3800 km and fringe spacing of 0.09 mas or 0.1 AU shows substantial compact structure.) Most of the luminosity of the source, $\sim$74%, arises from structures on scales greater than about 3 mas and hence are resolved by the interferometric array.

4.2. *Visibility Measurements of the Circumstellar Dust Shell*

The structure of the circumstellar shell, as traced by dust emission at 11.5 μm, has been resolved by the ISI on baselines of up to 32 m (Fig. 7). Danchi et al. (1994) present visibility data and discuss its calibration at projected baselines of up to 13 m and at an optical phase of 0.4. The addition here of data at 32 m permit the direct measurement of the photospheric emission, uncontaminated by dust shell emission. Furthermore, the addition of data at an optical phase of 0.9 permits the measurement of changes in the circumstellar dust shell during the stellar cycle. However, since the ISI is a two-element interferometer, no imaging was possible. Physical characteristics of the circumstellar dust shell were deduced by varying the

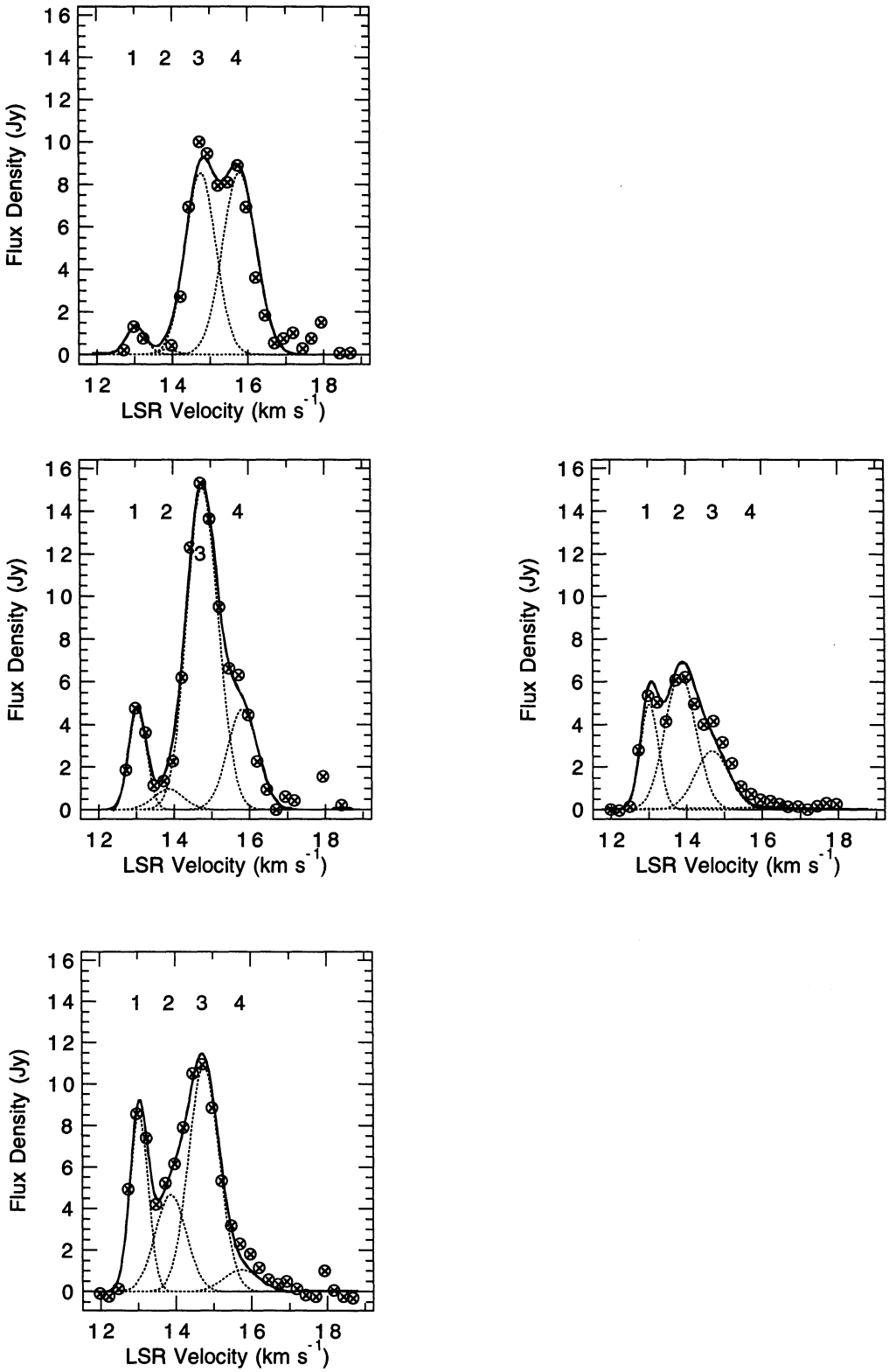

FIG. 4.—Spectral profiles for four closely spaced positions on the sky, obtained from the decomposition of the observed emission into four three-dimensional elliptical Gaussians in position and velocity. The accurate measurement of positions and mean velocities can be accomplished only by a three-dimensional analysis because of the overlap among features. The maser features are labeled 1–4. The spectra are arranged to reflect the relative positions of the corresponding pixels. The range of positions is about one beamwidth in R.A. and one half-beamwidth in declination. *Top left*: position offset (0.0, 0.8) mas; *middle left*: position offset (0.0, 0.0); *bottom left* position offset (0.2, −0.8); *middle right*: position offset (−0.6, 0.2).

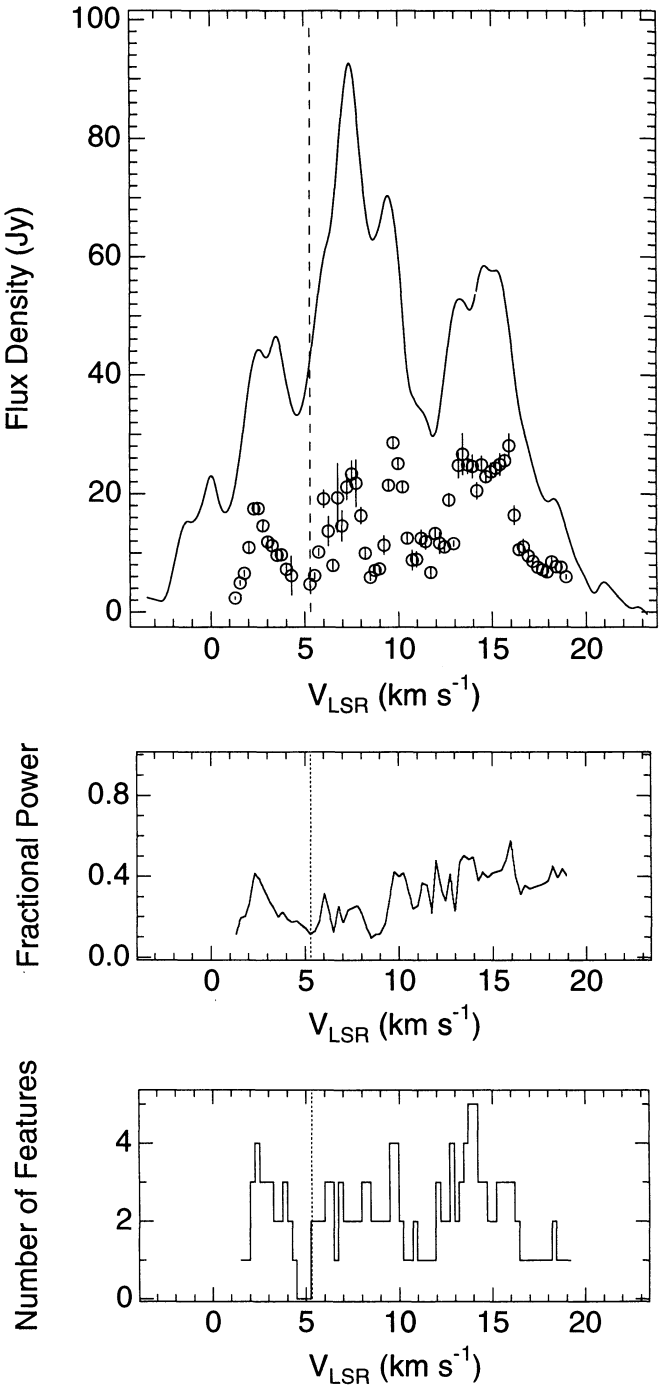

FIG. 5.—*Top*: Comparison of the total-power spectrum of the maser (*solid line*) to a spectrum of the power imaged with VLBI (*circles*). The adopted stellar velocity is denoted by the vertical dashed line. *Middle*: Fractional power imaged as a function of velocity. *Bottom*: histogram of the number of maser features detected for each spectral channel.

parameters in a radiative transfer model of a spherically symmetric shell so as to match the observed fringe visibilities as functions of projected baseline. The mid-infrared flux densities from these models were also matched to available spectroscopic data.

For VX Sgr near its optical minimum in 1992, and at about the same epoch as the VLBA observations, the radius at which the mid-infrared emission becomes significant is $\sim 4.6\ R_*$,

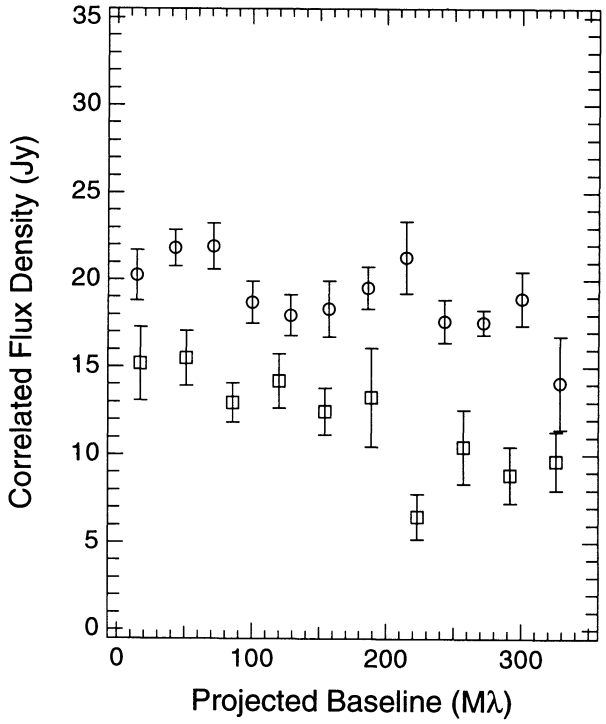

FIG. 6.—Fringe amplitude as a function of projected baseline length, in wavelengths, for two maser features. The upper trace is for the reference emission at 10.25 km s^{-1}, and the lower trace is for the weaker emission at 16.7 km s^{-1}. The data were averaged to 10 minutes and binned by baseline length to improve the S/N. Error bars denote the standard error in the average flux density in each bin. The flux densities of the features at 10.25 and 16.7 km s^{-1} are 51 and 31 Jy, respectively.

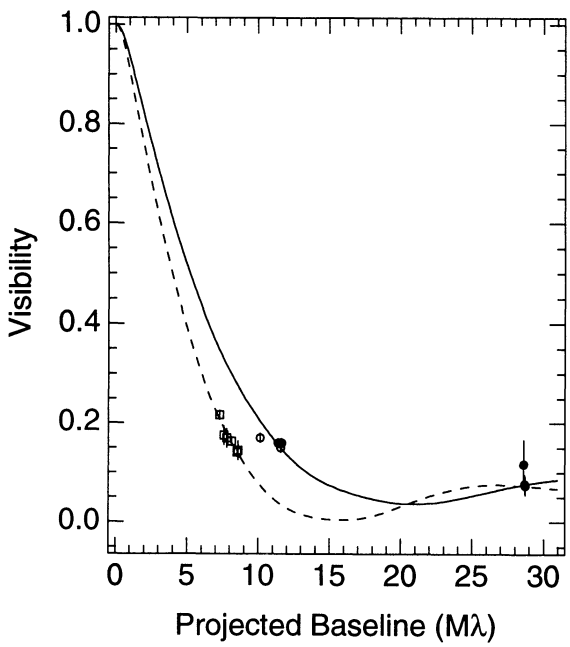

FIG. 7.—Visibility of the 11.5 μm emission from VX Sgr as a function of projected baseline in units of the wavelength. ISI data is shown for optical phases 0.4 (*open circles*), 0.9 (*open squares*), and 1.4 (*filled circles*). The visibilities predicted by a best-fit radiative transfer model are represented by the solid and dashed lines. We note that the long and short baseline data that correspond roughly to the stellar minimum were obtained during consecutive minima. The measured visibilities at baselines of $\sim 2.5 \times 10^5 \lambda$ were ~ 0.5, although these measurements cannot be compared in detail to the data shown here because they were made during earlier stellar cycles.

TABLE 3

DUST SHELL CHARACTERISTICS FROM IR INTERFEROMETRY

Parameter	Value
Stellar radius (R_*)	13 ± 2 mas
Shell inner radius[a]:	
(R_0^{min})	4.6 R_*
(R_0^{max})	6.0 R_*
H_2 density at R_0^{min} [b] [$n(H_2)$]	4.1×10^7 cm^{-3}
H_2 density at R_0^{max} [$n(H_2)$]	2.4×10^7 cm^{-3}
Shell mass[c] (M_{tot})	0.017 $M_\odot$

[a] Radius at which 11.15 μm emission by dust becomes significant. Here stellar minimum and maximum refer to optical phases of 0.4 and 0.9, respectively.

[b] Density declines from $n(H_2)$ by the square of the radius. In a thin layer close to R_0, the peak density is enhanced by 100% due to acceleration of dust by radiation pressure.

[c] Shell mass that lies within the 2".5 primary beam of the IR interferometer.

which is much larger than the radius of the maser shell, 1.3 R_*. The corresponding stellar radius is 13 ± 2 mas or 22 ± 3 AU (Fig. 7). The density profile of the dust is assumed to decrease as r^{-2}, where r is radius, except for an enhancement of about a factor of 2 due to acceleration by radiation pressure. Some characteristics of the model are listed in Table 3. Observations during the stellar minimum of 1994 with a 32 m baseline confirmed the stellar radius. For VX Sgr near its optical maximum in 1993, the inner radius was ~ 6.0 R_*. The substantial shift in the visibility of the star between the stellar minimum and maximum, which is shown in Figure 7, is clear evidence for a sizable change in the inner radius of the dust shell. Although no data that completely resolves the dust emission are available for the stellar maximum, the 13 mas stellar radius is consistent with the available moderate-resolution data.

5. DISCUSSION

5.1. *The Inner Radius of the Dust Shell*

The change in the innermost radius of 11.15 μm dust emission between optical phases of 0.4 and 0.9 is large and probably due to the destruction of dust by heating (Danchi et al. 1994). The temperature of the dust at the inner radius near stellar minimum is about 800 K. However, the changes could also be due to secular changes in the illumination of a clumpy dust shell. Observations by Dyck et al. (1984) made about 10 yr prior to the ISI observations show that dust emission and scattering at near-infrared wavelengths, which arise near the inner dust shell radius, become significant at a radius of about 2 R_*. However, they assumed a rather idealized Gaussian distribution for the near-infrared brightness. We do not think this difference in inner dust radii is significant because of the differences in wavelength and analysis techniques. However, we note that if dust generation were suppressed for the decade between the observations, then the inner dust shell boundary would have moved outward by 1.8 R_* for a flow velocity of 19 km s^{-1}. The stellar radius estimated from the ISI data is consistent with the 13 mas radius measured by Ridgway et al. (1977) using lunar occultation techniques.

5.2. *The Gas Density within the Dust Shell Inner Radius*

From the dust shell characteristics that are listed in Table 3, we estimate the H_2 density to be 10^9 cm^{-3} at the radius of the SiO maser emission. We have assumed a dust-to-gas ratio of 180, an inverse square law gas density profile, and a silicate dust composition. The H_2 density agrees with that expected in SiO maser regions, based on collisional and radiative excitation arguments (Elitzur 1992, p. 280). However, an inverse square density profile that fits the gas densities and radii at the inner edge of the dust shell and the maser regions is not consistent with typical photospheric densities of 10^{14}–10^{15} cm^{-3} (Draine 1981).

For a simple exponential stellar atmosphere with a density at the photosphere of 10^{14} cm^{-3} and a density at the radius of the dust shell of 4.1×10^7 cm^{-3}, the scale height would need to be about 0.2–0.3 R_*. Such an atmosphere would be several orders of magnitude more dense at the radius of the SiO emission than permitted without collisionally quenching the population inversion. Rather than the photospheric density, the relative densities of the SiO masers and the dust shell may be used to determine empirically the scale height of an exponential atmosphere over the region from 1.3 R_* to 4.6 R_*. If the SiO masers are collisionally excited with hydrogen densities of 10^9 cm^{-3}, and if the hydrogen density is 4.1×10^7 cm^{-3} at the inner edge of the dust shell, then an exponential atmosphere connecting the two densities would have a scale height of 1 R_*, significantly larger than the previous estimate. We note that this scale height is uncertain by about 0.3 because of intrinsic uncertainties in the contributing densities.

Results from the two methods of estimating the atmospheric scale height can be reconciled if pulsation-driven shock wave models of the atmospheres of these stars are applied to the present data (see Willson 1976; Fox & Wood 1985; Bertschinger & Chevalier 1985; Bowen 1988). These models describe how radial pulsations of the photosphere of the star create shocks in its atmosphere. Over time these shocks cause the atmospheres to be greatly extended compared to those of nonvariable stars. Bowen (1988) shows that the extension of the atmosphere increases strongly as the peak-to-peak amplitude of the pulsation velocity increases. This is also called the piston amplitude. As the piston amplitudes increase, the location where shocks form moves closer to the stellar photosphere. The region between the photosphere and where the shock is initiated has an exponential density profile with a scale height on the order 0.01 to 0.02 R_*. However, within the shocked atmosphere the exponential scale heights are at least an order of magnitude greater. Figure 1 of Bowen (1988) and Figure 1*b* of Cherchneff & Tielens (1994) can be used to determine scale heights for shocked atmospheres. For piston amplitudes in the range of 2–4 km s^{-1} these models give scale heights in the range of 0.6–0.7 R_*. This is close to the range of scale heights estimated from maser region and dust shell densities.

Physical conditions that are conducive to SiO maser emission other than gas density have been inferred for pulsation-driven stellar atmospheres. Based on time-series near-infrared spectroscopy Hinkle, Scharlach, & Hall (1984) estimate that the temperature and pulsation velocities force the maser emission region to lie outside the region in which shocks form in the cases of the nine Mira variable stars studied. Similar observations for χ Cyg by Hinkle, Hall, & Ridgway (1982) reveal the presence of a stationary layer of ejecta above the star, which acts as a reservoir for material that can fall toward the star under the influence of gravity, as well as for material that can be accelerated due to radiation pressure on condensing dust. However, our results for VX Sgr suggest that maser emission

may not arise in such a stationary layer, since it would probably lie closer to the radius of dust formation than the observed maser emission. Monitoring studies of SiO masers for several variable stars (Martínez et al. 1988) show that secondary maxima in the SiO maser light curves occur at about the same time as a line-doubling phase for the CO absorption lines. The line doubling occurs when infalling material from one cycle collides with the outward propagating shock from the following cycle (Hinkle 1978). Such a collision would occur inside the radius for the stationary layer. For the cycles of VX Sgr studied by Martínez et al. (1988), the secondary maximum has occurred at an optical phase of 0.8.

5.3. *The* SiO *Maser Shell*

The maser shell is close to, but above, the stellar photosphere of VX Sgr. The ringlike structure suggests gain paths that are tangent to the star, rather than along the line of sight to the star. This arrangement is not consistent with the proposal that circumstellar SiO masers lie within convective cells of the photosphere (Elitzur 1980). The geometry of the shell is similar to that observed for SiO masers associated with TX Cam and U Her (Diamond et al. 1994), and W Hya (Miyoshi et al. 1994). These shells may lie farther from the respective stellar photospheres, although no direct measurements of the stellar radii are available for them.

The strong redshifted center of maser activity along the southern limb of VX Sgr suggests the presence of organized asymmetric structure in the extended atmosphere, perhaps arising from uneven mass loss from the star. However, the maser emission may not be a good tracer of the mass in the envelope since the total molecular mass represented by the 36 maser features is on the order of only $6 \times 10^{-7}\ M_\odot$ (based on the assumption of cylindrical geometries, diameters of 0.4 AU, lengths of 1 R_*, and densities of 10^9 cm^{-3}). The total mass of the circumstellar envelope within the inner edge of the dust is much greater, about $7 \times 10^{-4}\ M_\odot$ (based on the assumption of densities of 10^{14} and 10^9 cm^{-3} for the photosphere and the maser regions, respectively, and exponential scale heights of 0.01 and 0.7 R_* inside and outside the radius of the maser emission, respectively). Danchi et al. (1994) estimate the total mass in the circumstellar shell of VX Sgr to be at least 0.02 $M_\odot$.

The locations of the clusters of maser features that are close in velocity to the stellar velocity do not suggest any specific velocity structure. The velocity dispersions within these clusters are a few km s^{-1}, which is the same order of magnitude as the sound speed for a gas temperature of 1000 K, and may be caused by turbulence. Polarization observations of 1612 MHz OH maser emission, which arises farther out in the circumstellar envelope, fix an upper limit on the strength of the magnetic field of $\sim$1 mG at a radius of 64 R_* (Cohen et al. 1987). Observations of the main-line OH maser emission indcate that the magnetic field has a strength of about 2 mG at a radius of 9 R_* (Chapman & Cohen 1986). For an inverse square dependence of field strength on radius, the magnetic field at the radius of the SiO maser emission shell would be about 0.1 G. The corresponding Alfvén wave velocity would be about 5 km s^{-1}, which would suggest that the magnetic field might play a significant role in the dynamics of the molecular gas. (Note that SiO is nonparamagnetic and the Zeeman splitting for this field would be on the order of only 10^4 km s^{-1}.)

It is commonly assumed that the acceleration of material in the circumstellar envelope begins at the radius where dust condensation occurs (Pijpers 1990; Zhiyao 1992). Prior estimates of the outflow and the acceleration have depended upon the trend of increasing velocity extents for circumstellar SiO, H_2O, and OH emissions, in that order (Chapman & Cohen 1986). The terminal velocity of the flow deduced from the velocity extent of the 1612 MHz OH masers at 64 R_* is 18.6 km s^{-1}. The work presented here provides additional indirect evidence for outflow close to the star, based on the density and location of the SiO maser region with respect to the inner edge of the dust shell. Note that the redshifted features along the southern limb (10–19 km s^{-1}) overlie two features that are blueshifted with respect to the stellar velocity (2.5 and 4.5 km s^{-1}). This superposition of velocity components may indicate the close proximity of both outflow and infall with velocities on the order of 10 km s^{-1}, although we cannot deduce the dynamics (i.e., outflow) of the maser features along the limb and outside the dominant southern cluster. The possibility of infall is particularly interesting in view of the infall of material inferred to take place around χ Cyg by Hinkle et al. (1982). Direct observations of the dynamics can be obtained by comparing several VLBI images that correspond to different optical phases within a single stellar cycle. At a distance of 1700 pc, a motion of 10 km s^{-1} corresponds to 1.2 mas yr^{-1}, which is large enough to be easily detected with multiple-epoch VLBI observations.

5.4. *Extended Maser Emission Outside the* SiO *Maser Shell*

The small ratios of imaged power to total power that are measured throughout the maser spectrum (Fig. 5) indicate that there is substantial extended structure resolved by the interferometer. However, the observed maser emission shows little indication of resolution within the range of fringe spacings of our interferometer array. The correlated flux densities as a function of projected baseline for two velocities at which there are only individual maser features present are shown in Figure 6. Though substantially less than unity, the equivalent visibilities are consistent with nearly unresolved source structure. As mentioned in § 4, for the channels where the S/N is sufficiently great we estimate that emission is confined in angle to less than about 0.2 mas, or 0.4 AU (FWHM). We note that the fractional power imaged should not be interpreted as a normalized visibility. It cannot be readily converted into an angular size by means of a Gaussian model brightness distribution because there is at least one spatial component responsible for the maser emission at most velocities (Fig. 5).

We suggest that VX Sgr exhibits SiO maser emission over a wide range of angular scales, with velocity coherence occurring on different scales in different parts of the circumstellar shell. With fringe spacings of about 0.6–20 mas (2323–72 km projected baseline length), we resolved with the VLBA all but the brightest, most compact emission, which traces the ringlike structure shown in Figure 3. We infer that there is maser emission on still larger scales from the high flux densities apparent in the total power spectrum (Fig. 2), the low correlated power of individual maser features (Fig. 5), and the very gradual decline in power as a function of fringe spacing (Fig. 6). It is not obvious where the larger scale emission arises, although the maximum angular scale is presumably fixed by the inner radius of the dust shell. However, we infer from the observations that in addition to a number of compact hot spots, a substantial fraction of the maser emission seen in the total-power spectrum must arise on angular scales that are comparable at least to the size of the star. The extended emission is concentrated toward the stellar velocity as is shown by the difference in the frac-

tional power imaged for velocities above and below ~ 10 km s^{-1}.

Previous VLBI observations of VX Sgr employed a 74 km baseline in 1978 and 1979. These observations had fringe spacings of about 30 mas, even longer than the largest obtained in the VLBA observations (Moran et al. 1979 and Lane 1982, 1984). In these previous observations about 60% of the overall maser luminosity was resolved. The reported visibilities were between $\lesssim 0.05$ and ~ 1, which indicated the presence of still more extended structure. In contrast to our results, the total angular extent of the maser source mapped in 1978–1979 was ~ 70 mas, and the morphology of the source was not ringlike (Lane 1982, 1984). We note that the SiO maser source has declined in strength by about a factor of 4 since 1979, which may be related to some variation in the rate of mass loss (see § 5.1). Hence, any comparisons should be made cautiously. We speculate that the velocity coherence of the circumstellar shell supports maser emission on scales as compact as 0.1 AU ($\sim 0.005\ R_*$), and on scales at least as extended as tens of AU ($\gtrsim 1\ R_*$), but smaller than the diameter of the dust shell ($< 4.6\ R_*$). An alternative conjecture is that each maser feature comprises a compact core and a halo, which contributes most of the flux density from the feature. VLBI observations with a broader range of baseline lengths will be necessary to resolve this ambiguity.

The presence of SiO maser emission on scales that approach the inner radius of circumstellar dust shell has been detected by lunar occultation measurements of the Mira-type variable star R Leo (Cernicharo et al. 1994). The SiO maser emission within 2 km s^{-1} of the stellar velocity arises from regions that are 40–60 mas in diameter and are separated by about 60 mas. The radius of the R Leo maser shell is 1–2 R_*, which is approximately the same as the shell radius for VX Sgr, although the stars are of different types. The uncertainty arises from stellar diameter measurements of 53 and 40 mas, at 11.15 μm by Danchi et al. (1994) and at 2.16 μm by Di Giacomo et al. (1991), respectively. The latter radius was corrected for limb darkening (Danchi et al. 1994).

6. SUMMARY

1. The first coordinated interferometric observations of a late-type star at millimeter and infrared wavelengths have been completed.

2. When observed with baselines in excess of 237 km, the SiO ($J = 1 \rightarrow 0$, $v = 1$) maser emission appears to lie in the extended stellar atmosphere, projected in a ringlike region of radius 1.3 R_*.

3. The compact maser emission lies well within 4.6 R_*, the radius at which mid-infrared dust emission from the circumstellar envelope becomes significant for a stellar phase of 0.4. At this phase the stellar radius is 22 ± 3 AU or 13 ± 2 mas. The dust radius has been estimated to be 6.0 R_* when the star is close to optical maximum.

4. The stellar atmosphere and mass loss, as traced by the masers, is asymmetric with a possible outflow or infall speed on the order of 10 km s^{-1}. The location of the maser shell and the estimated densities in the dust shell, maser shell, and photosphere constrain the scale height and density profile of the stellar atmosphere. The scale heights are consistent with models of pulsation-driven extension of the atmosphere by shocks.

5. The velocity structure of the maser source does not reveal any systematic velocity gradients but is consistent with turbulence of a few km s^{-1}, which is on the order of both the sound speed and the Alfvén speed. Magnetic fields may play a significant role in the dynamics of the circumstellar envelope close to the star.

6. Although the diameters of the masers that lie along the limb of the star are ~ 0.4 AU (0.02 R_*) there is significant emission on size scales almost an order of magnitude smaller (~ 0.1 AU) and at least an order of magnitude larger (> 30 AU). The diameter of the inner edge of the dust shell is probably the upper limit to the angular scale on which SiO maser emission can occur.

We thank C. H. Townes for helpful discussions and his support of this project. The UC Berkeley Infrared Spatial Interferometer is supported in part by grants from the Office of the Chief of Naval Research (N00014-89J-1583), and from the National Science Foundation (AST-9119317, AST-9221105, AST-9315485, AST-9321289). We also thank an anonymous referee for useful comments. J. Alcolea gave us archival SiO maser spectra made at the Yebes Observatory from 1985 to 1993. L. J. G. was supported by the Miller Institute for Basic Research in Science at the UC Berkeley during part of this work. F. C. acknowledges financial support from the Ministerio de Educación y Ciencia of Spain.

REFERENCES

Alcolea, J. 1993, private communication
Alter, G., Balázs, B., & Ruprecht, J., ed. 1970, Catalogue of Star Clusters and Associations (2d ed.; Budapest: Akad. Kiadó), 2379
Backer, D. C., Zensus, A. J., Kellermann, K. I., Reid, M. J., Moran, J. M., & Lo, K. Y. 1993, Science, 262, 1414
Bertschinger, E., & Chevalier, R. A. 1985, ApJ, 299, L167
Bowen, G. H. 1988, ApJ, 329, 299
Cernicharo, J., Brunswig, W., Paubert, G., & Liechti, S. 1994, ApJ, 423, L143
Chapman, J. M., & Cohen, R. J. 1986, MNRAS, 220, 513
Cherchneff, I., & Tielens, A. G. G. M. 1994, in Circumstellar Media in Late Stages of Evolution, ed. R. Clegg & I. Stevens (Cambridge: Cambridge Univ. Press), in press
Cohen, R. J., Downs, G., Emerson, R., Grimm, M., Gulkis, S., Stevens, G., & Tarter, J. 1987, MNRAS, 225, 491
Colomer, F., et al. 1992, A&A, 254, L17
Colomer, F., Menten, K. M., & Reid, M. J. 1995, in preparation
Danchi, W. C., Bester, M., Degiacomi, C. G., Greenhill, L. J., & Townes, C. H. 1994, AJ, 107, 1469
Diamond, P. J., Kemball, A. J., Junor, W., Zensus, A., Benson, J., & Dhawan, V. 1994, ApJ, 430, L61
Dickinson, D. F., Reid, M. J., Morris, M., & Redman, R. 1978, ApJ, 220, L113
Di Giacomo, A., Richichi, A., Lisi, F., & Calamai, G. 1991, A&A, 249, 397
Draine, B. T. 1981, in Physical Processes in Red Giants, ed. I. Iben, Jr. & A. Renzini (Dordrecht: Reidel), 317
Dyck, H. M., Zuckerman, B., Leinert, Ch., & Beckwith, S. 1984, ApJ, 287, 801
Elitzur, M. 1980, ApJ, 240, 553
———. 1992, Astronomical Masers (Boston: Kluwer)
Eubanks, M., & Walker, R. C. 1993, private communication
Fox, M. W., & Wood, P. R. 1985, ApJ, 297, 455
Greenhill, L. J., Moran, J. M., Backer, D. C., Bester, M., & Danchi, W. C. 1994, in Amplitude and Intensity Interferometry III, ed. J. B. Breckinridge (Bellingham: SPIE), 2200, 304
Greenhill, L. J., Moran, J. M., Reid, M. J., Menten, K. M., & Hirabayashi, H. 1993, ApJ, 406, 482
Haniff, C. A., Ghez, A. M., Gorham, P. W., Kulkarni, S. R., Matthews, K., & Neugebauer, G. 1992, AJ, 103, 1662
Hinkle, K. H. 1978, ApJ, 220, 210
Hinkle, K. H., Hall, D. N. B., & Ridgway, S. T. 1982, ApJ, 252, 697
Hinkle, K. H., Schlarlach, W. W. G., & Hall, D. N. B. 1984, ApJS, 56, 1
Humphreys, R. M. 1974, ApJ, 188, 75
Humphreys, R. M., Strecker, D. W., & Ney, E. P. 1972, ApJ, 172, 75

Kholopov, P. N., et al. 1987, General Catalogue of Variable Stars, (4th ed.; Moscow: Nauka)
Lane, A. P. 1982, Ph.D. dissertation, Univ. Masschusetts, Amherst
———. 1984, in IAU Symp. 110, VLBI and Compact Radio Sources, ed. R. Fanti, K. I. Kellermann, & G. Setti (Dordrecht: Reidel), 329
Loup, C., Forveille, T., Omont, A., & Paul, J. F. 1993, A&AS, 99, 291
Martínez, A., Bujarrubal, V., & Alcolea, J. 1988, A&AS, 74, 273
McIntosh, G. C., Predmore, C. R., Moran, J. M., Greenhill, L. J., Reid, M. J., Rogers, A. E. E., & Barvanis, R. E. 1989, ApJ, 337, 934
Miyoshi, M., Matsumoto, K., Kameno, S., Takaba, H., & Iwata, T. 1994, Nature, 371, 395
Moran, J. M., Ball, J. A., Predmore, C. R., Lane, A. P., Huguenin, G. R., Reid, M. J., & Hansen, S. S. 1979, ApJ, 231, L67
Pijpers, F. P. 1990, A&A, 238, 256
Reid, M. J., Haschick, A. D., Burke, B. F., Moran, J. M., Johnston, K. J., & Swenson, G. W. 1980, ApJ, 239, 89
Reid, M. J., & Moran, J. M. 1988, in Galactic and Extragalactic Radio Astronomy, ed. G. Verschuur & K. I. Kellermann (Berlin: Springer), 255
Ridgway, S. T., Wells, D. C., & Joyce, R. R. 1977, AJ, 82, 414
Thompson, A. R., Moran, J. M., & Swenson, G. W., Jr. 1986, Interferometry and Synthesis in Radio Astronomy (New York: Wiley)
Wallerstein, G. 1977, ApJ, 211, 170
Wallerstein, G., & Fawley, W. M. 1980, PASP, 92, 183
Willson, L. A. 1976, ApJ, 205, 172
Wilson, R. W., Baldwin, J. E., Buscher, D. F., & Warner, P. J. 1992, MNRAS, 257, 369
Wright, M. C. H., Carlstrom, J. E., Plambeck, R. L., & Welch, W. J. 1990, AJ, 99, 1299
Zhiyao, Y. 1992, Ap&SS, 192, 53